Masked Autoencoding (MAE) Outperforms Joint-Embedding Prediction (JEPA) for Frozen-Probe Very-High-Resolution Landslide Segmentation

Sansar Raj Meena[1,2,3], Xiaochuan Tang[4,5], and Filippo Catani[2]

[1]National Institute of Oceanography and Applied Geophysics – OGS, Borgo Grotta Gigante 42/C, Sgonico, Italy

[2]Department of Geosciences, University of Padua, Padua, 35129, Italy

[3]Center for Remote Sensing, Department of Earth and Environment, Boston University, Boston, MA, USA

[4]State Key Laboratory of Geohazard Prevention and Geoenvironment Protection, Chengdu University of Technology, Chengdu, 610059, China

[5]College of Computer Science and Cyber Security, Chengdu University of Technology, Chengdu, 610059, China

Correspondence: smeena@ogs.it

This is a non-peer-reviewed preprint submitted to **EarthArXiv** *(eartharxiv.org).*
It is intended for submission to a peer-reviewed journal; this record will be updated with the journal reference and DOI if and when the article is published.

ORCID (submitting author, S.R. Meena): https://orcid.org/0000-0001-6175-6491

Keywords: self-supervised learning; masked autoencoder; joint-embedding predictive architecture; landslide mapping; very-high-resolution remote sensing; semantic segmentation; Emilia-Romagna

Abstract

Mapping landslides from very-high-resolution (VHR) imagery is central to regional hazard assessment, yet supervised segmentation is constrained by the cost of expert pixel-level annotation. Self-supervised learning can exploit large unlabeled aerial archives, but which pretext objective best captures landslide morphology is unknown. Using a regional inventory from the 2023 Emilia-Romagna rainfall event, we compare two self-supervised objectives—masked autoencoding (MAE) and joint-embedding prediction (JEPA)—trained from scratch on 4.85 million unlabeled 0.2 m aerial patches and evaluated under an identical frozen-encoder protocol across label fractions from 1% to 100%. Although joint-embedding prediction has been reported to surpass masked reconstruction on ImageNet linear probing, low-label classification, and low-level tasks such as depth and counting, we find that MAE outperforms JEPA at every label fraction under this dense-segmentation protocol, and multiseed repeats confirm that the gap exceeds decoder-probe seed variance by roughly fifteenfold at the smallest label fraction and sixfold at full labels. In-domain masked pretraining reaches 3.16 times the landslide-class IoU of an architecture-matched randomly initialized frozen encoder, and controls show that the advantage cannot be explained by decoder training alone. Under a matched frozen-encoder protocol, MAE is comparable to a strong ADE20k-supervised SegFormer-B2 encoder at the smallest label fraction and clearly surpasses it as labels increase, as the supervised encoder's frozen features saturate; an end-to-end fine-tuned SegFormer-B2, reported as a strong externally pretrained reference, remains higher. These results situate masked reconstruction as a representation that better encodes the fine morphology relevant to label-efficient VHR landslide mapping.

1 Introduction

Landslides are among the most damaging geomorphic hazards, producing loss of life, infrastructure disruption, sediment cascades, and long-lasting landscape change [1, 2]. Their frequency and impact are rising as extreme-rainfall events intensify in mountainous terrain: the May 2023 Emilia-Romagna event in the northern Italian Apennines, for example, triggered tens of thousands of shallow landslides across a single region within days, overwhelming conventional mapping capacity. Accurate landslide inventories underpin emergency response, susceptibility modelling, hazard assessment, risk mitigation, and the interpretation of such triggering events. Remote sensing has greatly expanded the spatial scale at which landslides can be mapped, but reliable inventories still depend largely on expert image interpretation, which remains a bottleneck precisely when landslides are most numerous, spatially dispersed, and triggered under time-critical post-event conditions—the conditions under which hazard information is most urgently needed.

Automated landslide identification has undergone a paradigm shift, moving from expert-designed features and classical classifiers toward deep representation learning. Early feature-based studies relied on hand-crafted spectral, textural, and morphometric features with rule-based or classical classifiers for landslide delineation [3, 4]. Subsequently, data-driven paradigms became increasingly dominant, progressing from classical machine learning to deep-learning models capable of end-to-end representation learning [5, 6]. Deep learning has further advanced through successive architectural innovations, from convolutional neural networks [7] to Transformers [8], CNN–Transformer hybrids [9], and more recently Mamba-based models [10, 11], continually pushing the accuracy ceiling of landslide detection. Most studies have focused on optimizing model design, including multi-scale feature fusion [12], multimodal feature integration [13], and lightweight architectures [14]. Landslide4Sense established a reference benchmark for multisource landslide detection and standardized deep-learning evaluation in the domain [15], while Nava et al. [16] used Sentinel-1 SAR to detect co-seismic landslides across globally distributed events and Tang et al. [17] introduced vertical federated learning to address the institutional fragmentation of high-resolution geohazard data. Yet these architectural gains have largely been achieved within supervised, task-specific models, whose accuracy is constrained by the availability of dense expert annotations. Such dependence makes landslide mapping costly, sensitive to class imbalance, and poorly transferable across regions, sensors, land-cover settings, and landslide types. Three persistent challenges follow. Pixel-level landslide masks require geomorphic expertise and careful interpretation of complex terrain; landslide pixels are rare relative to background, so models must learn small, irregular foreground objects under severe imbalance; and models trained in one region or sensor regime often degrade under other acquisition geometries, land covers, or landslide types.

To address this annotation bottleneck, transfer learning has been explored as a practical route to label-efficient landslide detection, transferring source-domain knowledge to label-scarce target regions. This is commonly achieved by pretraining detection networks on external data, from generic visual datasets such as ImageNet [18], including for non-nadiral and crowdsourced landslide imagery [19], to more task-relevant labeled landslide datasets, including HR-GLDD [20], CAS Landslide [21], GDCLD [22], LMHLD [23], and Landslide4Sense [15], which provide high-quality source-domain priors. Several studies have reduced the demand for annotated target samples by pretraining landslide-detection networks on task-relevant landslide datasets [24, 25], and SAM-based foundation-model frameworks have extended this idea into multi-stage transfer paradigms for few-shot landslide detection [26–28]. Nevertheless, these transfer-oriented paradigms remain constrained by the source knowledge they depend on: generic pretraining datasets are only weakly related to landslide morphology, whereas existing landslide-specific datasets remain limited in scale, diversity, and encoded geomorphic knowledge. This gap is critical because effective landslide representations must preserve fine boundary and texture cues while remaining robust to complex non-landslide backgrounds. Self-supervised learning offers a promising but still underexplored alternative, as it can exploit abundant unlabeled remote-sensing archives to learn task-relevant representations before any supervised fine-tuning.

Two prominent families of masked-prediction pretext objectives structure current SSL, alongside contrastive and self-distillation approaches. Masked image modelling, exemplified by the masked autoencoder (MAE), trains a network to reconstruct masked image content from visible context and scales efficiently to large corpora [29–31]. These methods were introduced on the Vision Transformer backbone [32] and follow an earlier line of contrastive self-supervised learning [33, 34]. Joint-embedding predictive architectures (JEPA) instead predict the representations of masked regions in a learned feature space, an objective designed to encourage semantic abstraction while avoiding low-level reconstruction [35]; this lineage builds on self-distillation approaches such as DINO, whose features were shown to encode semantic structure useful for dense prediction [36] and which scale to general-purpose visual features under large-scale curated pretraining [37]. In Earth observation, SSL has been adapted to multispectral, multitemporal, and multiscale satellite imagery through contrastive in-domain pretraining such as Seasonal Contrast [38] and large multimodal pretraining corpora [39], and through masked-image-modelling approaches including SatMAE [40], Scale-MAE [41], and large geospatial models such as Prithvi-EO-2.0 [42]. Joint-embedding prediction has also begun to reach Earth observation: AnySat adapts a JEPA-style objective across heterogeneous EO resolutions and modalities [43], and REJEPA applies joint-embedding prediction to remote-sensing representation learning [44]. However, most geospatial SSL is oriented toward satellite-resolution semantic interpretation and broad land-cover transfer, and no controlled comparison of masked pixel reconstruction against joint-embedding prediction exists for frozen-probe VHR landslide segmentation.

VHR aerial landslide segmentation differs in ways that make the choice of objective an open scientific question rather than a settled import. Decimetric imagery exposes fine geomorphic features — scar boundaries, debris textures, disrupted vegetation, drainage disruption, road-cut failures, shallow translational slides — and the foreground class is sparse. The published evidence favouring feature-space prediction is concentrated on image classification under linear probing and on low-level tasks such as depth estimation and object counting [35]; on dense semantic segmentation, reconstruction-based objectives have remained strongly competitive. Whether suppressing pixel-level reconstruction helps or hurts the representation of fine landslide morphology has not been tested under a controlled downstream landslide protocol.

Here we resolve this question for VHR landslide segmentation through a controlled comparison, and the answer runs counter to the transfer behaviour reported on classification-oriented benchmarks. Trained from scratch on millions of unlabeled VHR aerial-image patches and evaluated under an identical frozen-encoder protocol, does masked reconstruction or joint-embedding prediction yield representations that better support label-efficient landslide mapping? Although joint-embedding prediction has been reported to match or surpass masked reconstruction on ImageNet linear probing, low-label classification, and low-level prediction tasks, we find that masked reconstruction produces consistently stronger representations for dense VHR landslide segmentation at every label fraction. The answer bears directly on how the geoscience community should build the next generation of self-supervised models for high-resolution hazard mapping, where labels are scarce but unlabeled imagery is abundant. We frame the contribution conservatively as domain-specialized VHR representation learning rather than a general Earth-observation foundation model, a broader claim that would require multi-region, multi-sensor, and multi-task evidence beyond the present scope.

The main contributions are as follows. First, we train MAE and JEPA encoders from scratch on the same 4,848,151-patch unlabeled VHR aerial corpus. Second, we evaluate both under an identical frozen-encoder UPerNet protocol over six nested label fractions on a large VHR landslide benchmark. Third, we quantify stability through multiseed decoder-probe experiments at the 1% and 100% fractions. Fourth, we control checkpoint-selection bias by fixing the primary checkpoint before the downstream sweep and reporting a post hoc checkpoint only as sensitivity. Fifth, we verify the architecture path used in single-frame probing, showing numerically that the hybrid pretrained block reduces exactly to its spatial pathway at $T = 1$. Sixth, we report control experiments — a randomly initialized frozen encoder and a final-layer-only feature-tap ablation — that test whether decoder capacity or multi-level feature extraction explains the observed performance. Finally, we interpret why pixel-space reconstruction may be better aligned than feature-space prediction with VHR landslide morphology.

Table 1: Per-epoch composition of the unlabeled VHR pretraining corpus. The six acquisition epochs span 47 years (1976–2023) over the same Emilia-Romagna terrain; all are three-channel RGB at 512×512 px and 0.2 m resolution. The 2023 epoch is the single epoch shared with the labeled benchmark.

Acquisition epoch	Patches	Share
1976	753,888	15.6%
2008	756,022	15.6%
2011	765,416	15.8%
2018	743,382	15.3%
2020	764,789	15.8%
2023	1,064,654	22.0%
Total	4,848,151	100%

2 Study Area and Data

2.1 Unlabeled VHR pretraining corpus

MAE and JEPA were trained from scratch on 4,848,151 unlabeled RGB aerial-image patches stored in 2,033 WebDataset shards. Patches are 512×512 pixels at 0.2 m spatial resolution, corresponding to approximately $102.4\,\mathrm{m}\times102.4\,\mathrm{m}$ of ground coverage, and each sample is paired with metadata and a per-patch acquisition-year entry. The pretraining corpus was used without landslide labels, and downstream evaluation was performed on a fixed labeled benchmark.

The corpus is multi-epoch: it draws on six aerial acquisition epochs of the same Emilia-Romagna terrain—1976, 2008, 2011, 2018, 2020, and 2023—spanning 47 years (Table 1). A sampled modality audit confirmed that patches from all six epochs, including the 1976 acquisition, are stored as three-channel RGB imagery with non-identical channels rather than as replicated grayscale. The five historical epochs each contribute on the order of 0.75 million patches, while the 2023 epoch—concurrent with the labeled benchmark—contributes about 1.06 million. This near-half-century span is what distinguishes the corpus from single-epoch landslide pretraining resources: over decades, the same slopes undergo vegetation regrowth, land-use change, and successive failure and stabilization, so the unlabeled imagery encodes how landslide-prone terrain appears under markedly different surface conditions rather than at a single moment. The acquisitions are six discrete epochs, not continuous annual coverage; the long gap between the 1976 and 2008 epochs reflects the availability of historical orthophotography for the region.

2.2 Supervised landslide segmentation benchmark

Downstream probing uses a VHR landslide benchmark derived from the RER2023 Emilia-Romagna inventory [45]. The May 2023 rainfall episode triggered widespread shallow failures across the Apennine foothills of the Emilia-Romagna region in northern Italy (Figure 1), motivating compilation of the dense, high-resolution inventory from which the benchmark is derived. The benchmark contains 449,153 image–mask pairs: 381,719 training pairs and 67,434 validation pairs. Across all samples it comprises 117,742,764,032 labeled pixels, including 5,721,352,695 landslide pixels and 112,021,411,337 background pixels. The positive landslide fraction is 4.8592%, and 248,076 patches (55.232%) contain no landslide pixels. This imbalance reflects the regional rarity of landslide areas and motivates foreground-class IoU and F1 as the primary metrics rather than overall accuracy.

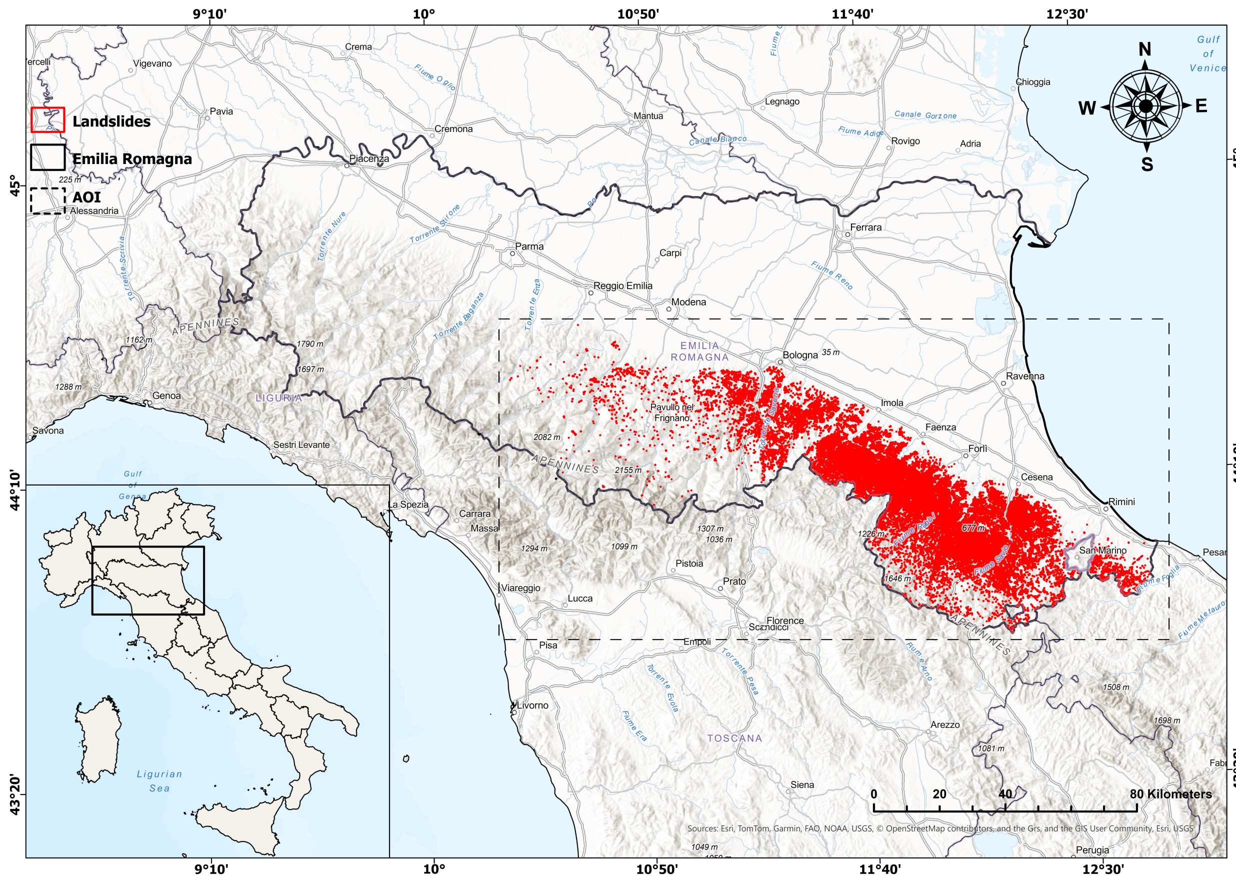

Figure 1: Study area. Location of the RER2023 Emilia-Romagna VHR landslide benchmark in northern Italy. Red points mark landslides of the May 2023 rainfall-triggered episode across the Apennine foothills, the solid outline delineates the Emilia-Romagna administrative boundary, and the dashed rectangle marks the area of interest (AOI); the inset locates the study area within Italy. The same regional footprint provides the unlabeled multi-temporal aerial archive used for self-supervised pretraining. Basemap sources: Esri, TomTom, Garmin, FAO, NOAA, USGS, © OpenStreetMap contributors, and the GIS User Community.

3 Methods

3.1 Overview

Figure 2 summarizes the workflow. MAE and JEPA are trained on the same unlabeled VHR corpus and evaluated under the same downstream protocol: the encoder is frozen, intermediate features are extracted from four depths, and a trainable UPerNet decoder [46] predicts binary landslide masks. This design isolates representation quality from end-to-end supervised adaptation.

3.2 Self-supervised representation learning: definition and mechanism

Supervised segmentation learns a mapping directly from images to expert-drawn masks, so the quality of the learned representation is bounded by the quantity of annotation available. Self-supervised learning (SSL) reduces this dependence at the representation stage: representation quality remains bounded by data coverage, architecture, objective, and compute, but no longer by annotation volume. Given an unlabeled image corpus $\mathcal{D}_u = \{\mathbf{x}^{(i)}\}_{i=1}^{N_u}$, SSL constructs a *pretext task* whose supervisory signal is generated from the data itself: part of each image is withheld, and the network is trained to recover the withheld part from the remaining context. Because the target is derived from the input rather than from a human annotator, the objective can be scaled to the full size of an archive—here $N_u = 4{,}848{,}151$ patches—at no annotation cost.

Formally, let $f_\theta : \mathbb{R}^{H\times W\times 3} \rightarrow \mathbb{R}^{N\times D}$ denote an encoder with parameters θ mapping an image to N token embeddings of width D. SSL optimises

$$\theta^\star = \arg\min_{\theta,\psi}\ \mathbb{E}_{\mathbf{x}\sim\mathcal{D}_u}\ \mathcal{L}_{\text{pretext}}\big(h_\psi(f_\theta(\mathcal{T}(\mathbf{x}))),\ \mathcal{Y}(\mathbf{x})\big), \tag{1}$$

where $\mathcal{T}(\cdot)$ is a corruption operator (here, token masking), h_ψ is an auxiliary head discarded after pretraining, and $\mathcal{Y}(\mathbf{x})$ is the self-generated target. The two objective families compared in this study differ principally in the space in which $\mathcal{Y}$ is defined. In masked reconstruction (MAE), $\mathcal{Y}$ is the raw pixel content of the masked patches, so the loss is computed in input space and the encoder is penalised for discarding any information required to redraw the missing texture. In joint-embedding prediction (JEPA), $\mathcal{Y}$ is the embedding of the masked region produced by a slowly updated copy of the encoder, so the loss is computed in representation space; content that the target encoder itself does not represent incurs no penalty, which by design permits—and encourages—the suppression of low-level detail.

After pretraining, h_ψ is discarded and $f_{\theta^\star}$ is transferred to the downstream task. In a *frozen-probe* evaluation the transferred encoder receives no gradient: θ is held at $\theta^\star$ and only a lightweight decoder is trained. Downstream accuracy is then a direct readout of what Eq. (1) caused the encoder to retain, which is precisely the quantity this study compares between the two objectives.

3.3 ChronoSat encoder and single-frame architecture audit

We refer to the pretrained backbone as the ChronoSat encoder throughout. The name denotes a hybrid spatial–temporal architecture designed for chronologically diverse Earth-observation imagery; despite the "Sat" element, the corpus used here consists of 0.2 m aerial orthophotos rather than satellite acquisitions, and only the spatial pathway is exercised downstream ($T = 1$; Section 3.3).

3.3.1 Tokenisation and notation

The encoder, both pretraining objectives, and all downstream probes are implemented in PyTorch with selective-scan kernels from the `mamba-ssm` library; the unlabeled corpus is streamed from 2,033 WebDataset shards, and all runs use `bfloat16` mixed precision on NVIDIA H100 80 GB GPUs (Table 2). A single-frame input $\mathbf{X} \in \mathbb{R}^{H \times W \times 3}$ with $H = W = 512$ is partitioned into non-overlapping square patches of side $p = 16$, giving a token grid of side $h = w = H/p = 32$ and $N = hw = 1024$ tokens. Each patch is linearly embedded and augmented with a learned positional code:

$$\mathbf{z}_n^{(0)} = \mathbf{E}\,\mathrm{vec}(\mathbf{X}_n) + \mathbf{p}_n, \qquad \mathbf{E} \in \mathbb{R}^{D \times 3p^2}, \quad n = 1, \dots, N, \tag{2}$$

with embedding width $D = 1280$. For multi-temporal input the tensor carries an additional axis T, and tokens are indexed $\mathbf{z}_{t,n}^{(0)}$ with $t = 1, \dots, T$. All downstream segmentation probes operate on independently sampled single RGB patches ($T = 1$): in the probing architecture the temporal/Mamba components are stripped and the temporal checkpoint keys are discarded when the MAE and JEPA encoders are loaded. The self-supervised pretraining corpus is organized as single-patch RGB samples with JSON metadata and acquisition-year sidecars, and both MAE and JEPA pretraining operate on these single patches ($T = 1$); no multi-frame temporal sequences are constructed at any stage. The multi-epoch signal therefore enters through acquisition-year diversity across the unlabeled corpus (Table 1) rather than through multi-frame temporal modelling, and the temporal/state-space pathway is inactive in both pretraining and probing.

3.3.2 Hybrid encoder block

The encoder stacks $L = 48$ identical hybrid blocks. Each block applies a pre-normalised spatial pathway followed by a conditionally executed temporal pathway:

$$\mathbf{u}^{(\ell)} = \mathbf{z}^{(\ell-1)} + \mathrm{MHSA}\big(\mathrm{LN}(\mathbf{z}^{(\ell-1)})\big), \tag{3}$$

$$\mathbf{v}^{(\ell)} = \mathbf{u}^{(\ell)} + \mathrm{FFN}_{\mathsf{SwiGLU}}\big(\mathrm{LN}(\mathbf{u}^{(\ell)})\big), \tag{4}$$

$$\mathbf{z}^{(\ell)} = \mathbf{v}^{(\ell)} + \mathbf{1}[\,T > 1\,] \cdot \mathrm{SSM}\big(\mathrm{LN}(\mathbf{v}^{(\ell)})\big). \tag{5}$$

Spatial mixing. MHSA is standard multi-head self-attention over the N spatial tokens with $H_a = 16$ heads and head width $d_k = D/H_a = 80$:

$$\mathrm{head}_i = \mathrm{softmax}\!\left(\frac{\mathbf{Q}_i \mathbf{K}_i^\top}{\sqrt{d_k}}\right)\mathbf{V}_i, \qquad \mathbf{Q}_i = \mathbf{Z}\mathbf{W}_i^Q,\ \mathbf{K}_i = \mathbf{Z}\mathbf{W}_i^K,\ \mathbf{V}_i = \mathbf{Z}\mathbf{W}_i^V, \tag{6}$$

$$\mathrm{MHSA}(\mathbf{Z}) = \big[\mathrm{head}_1 \,\|\, \cdots \,\|\, \mathrm{head}_{H_a}\big]\mathbf{W}^O, \qquad \mathbf{W}^O \in \mathbb{R}^{D \times D}. \tag{7}$$

Attention is computed over spatial positions only; no token is attended across the temporal axis, which is handled exclusively by the state-space pathway of Eq. (5).

Channel mixing. The feed-forward sublayer uses a gated SwiGLU nonlinearity,

$$\mathrm{FFN}_{\mathsf{SwiGLU}}(\mathbf{z}) = \mathbf{W}_2\Big(\mathrm{SiLU}(\mathbf{W}_g\mathbf{z}) \odot (\mathbf{W}_1\mathbf{z})\Big), \qquad \mathrm{SiLU}(a) = a\,\sigma(a), \tag{8}$$

with $\mathbf{W}_g, \mathbf{W}_1 \in \mathbb{R}^{d_{\mathrm{ff}} \times D}$ and $\mathbf{W}_2 \in \mathbb{R}^{D \times d_{\mathrm{ff}}}$, where d_{ff} is the feed-forward expansion width, $\sigma(\cdot)$ is the logistic sigmoid, and $\odot$ denotes the elementwise product.

Temporal mixing. The temporal pathway is a selective state-space model (Mamba) [47, 48] applied independently at each spatial position along the temporal axis. For a scalar input stream x_t at one position and channel, the underlying continuous system

$$\frac{\mathrm{d}\mathbf{h}(t)}{\mathrm{d}t} = \mathbf{A}\mathbf{h}(t) + \mathbf{B}x(t), \qquad y(t) = \mathbf{C}^\top \mathbf{h}(t) + D_{\mathrm{skip}} x(t), \tag{9}$$

is discretised with a zero-order hold at input-dependent step size $\Delta_t = \mathrm{softplus}(\mathbf{w}_\Delta^\top \mathbf{z}_t)$:

$$\bar{\mathbf{A}}_t = \exp(\Delta_t \mathbf{A}), \qquad \bar{\mathbf{B}}_t = (\Delta_t \mathbf{A})^{-1}\big(\exp(\Delta_t \mathbf{A}) - \mathbf{I}\big)\, \Delta_t \mathbf{B}_t, \tag{10}$$

yielding the recurrence

$$\mathbf{h}_t = \bar{\mathbf{A}}_t \mathbf{h}_{t-1} + \bar{\mathbf{B}}_t x_t, \qquad y_t = \mathbf{C}_t^\top \mathbf{h}_t + D_{\mathrm{skip}} x_t, \qquad \mathbf{h}_0 = \mathbf{0}. \tag{11}$$

Selectivity refers to Δ_t, $\mathbf{B}_t$, and $\mathbf{C}_t$ being functions of the token content rather than fixed, which allows the state to gate what is propagated across acquisition epochs.

3.3.3 Single-frame architecture audit

The downstream task is single-frame VHR landslide segmentation, so all probes are evaluated at $T = 1$. The equivalence between the full hybrid block and its spatial pathway at $T = 1$ is established analytically by the explicit gate: the indicator $\mathbf{1}[T > 1]$ in Eq. (5) disables the state-space branch for a singleton temporal axis, so the block collapses to

$$\mathbf{z}^{(\ell)}\Big|_{T=1} = \mathbf{v}^{(\ell)} = \mathbf{u}^{(\ell)} + \mathrm{FFN}_{\mathsf{SwiGLU}}\big(\mathrm{LN}(\mathbf{u}^{(\ell)})\big), \tag{12}$$

i.e. the pre-norm attention and SwiGLU sublayers alone. We note that the gate is what establishes the equivalence: a length-one state-space evaluation would otherwise still produce a non-zero output through $\mathbf{h}_1 = \bar{\mathbf{B}}_1 x_1$ and $y_1 = \mathbf{C}_1^\top \mathbf{h}_1 + D_{\mathrm{skip}} x_1$. As implementation verification of this execution path, we compared full-block and spatial-only outputs on identical inputs at $T = 1$ and obtained zero maximum absolute and zero maximum relative difference, $\max\left|\mathbf{z}_{\mathsf{full}} - \mathbf{z}_{\mathsf{spatial}}\right| = 0$. The frozen-probe implementation accordingly excludes the inactive temporal/state-space parameters at checkpoint load time. The spatial pathway evaluated downstream comprises approximately 8.67×10^8 parameters, while the full checkpoint additionally stores the temporal/state-space parameters that are inactive at $T = 1$; reported parameter counts refer to the spatial path unless stated otherwise.

3.3.4 Multi-level feature taps and decoder interface

Hidden states are read from blocks $\ell \in \{11, 23, 35, 47\}$ (zero-indexed, so layer 47 is the final of the 48 blocks) and reshaped from token sequences to spatial feature maps,

$$\mathbf{F}^{(\ell)} = \mathrm{reshape}\big(\mathbf{z}^{(\ell)}\big) \in \mathbb{R}^{32\times 32\times 1280}, \tag{13}$$

then projected to the feature-pyramid width $C_{\mathrm{FPN}} = 512$ and resampled to the pyramid scales expected by the UPerNet decoder [46]. UPerNet applies pyramid pooling to the deepest level, fuses the pyramid top-down, concatenates the fused levels, and predicts two-class logits that are bilinearly upsampled to the input resolution:

$$\hat{\mathbf{Y}} = \mathrm{Up}_{\times p}\Big(\mathrm{Conv}_{1\times 1}\big(\mathrm{Fuse}\big(\mathbf{F}^{(11)}, \mathbf{F}^{(23)}, \mathbf{F}^{(35)}, \mathrm{PPM}(\mathbf{F}^{(47)})\big)\big)\Big) \in \mathbb{R}^{512\times 512\times 2}. \tag{14}$$

During probing, only the decoder parameters entering Eq. (14) receive gradients; the encoder parameters θ in Eqs. (2)–(13) are frozen.

3.4 MAE and JEPA pretraining

Both objectives instantiate Eq. (1) on the same unlabeled corpus with the same encoder family and the same downstream probe architecture; neither model is initialized from ImageNet or any external Earth-observation model. Implementation settings are summarized in Table 2.

MAE. A random subset $\mathcal{M} \subset \{1, \ldots, N\}$ of patch tokens with masking ratio $|\mathcal{M}|/N = 0.75$ is removed; the encoder sees only the visible tokens, and an eight-layer reconstruction decoder predicts the missing pixel content [29]. The loss is the mean squared error over masked patches only:

$$\mathcal{L}_{\mathrm{MAE}} = \frac{1}{|\mathcal{M}|} \sum_{n\in\mathcal{M}} \big\|\hat{\mathbf{x}}_n - \mathbf{x}_n\big\|_2^2. \tag{15}$$

JEPA. A context encoder f_θ and a predictor g_ψ predict the representations of masked target blocks produced by a target encoder $f_{\bar\theta}$ whose weights are an exponential moving average (EMA) of θ [35]:

$$\mathcal{L}_{\mathrm{JEPA}} = \frac{1}{|\mathcal{B}|} \sum_{b\in\mathcal{B}} \big\|g_\psi\big(f_\theta(\mathbf{x}_{\mathrm{ctx}}),\, \mathbf{m}_b\big) - \mathrm{sg}\big[f_{\bar\theta}(\mathbf{x})_b\big]\big\|_2^2, \qquad \bar\theta \leftarrow \tau\bar\theta + (1-\tau)\theta, \tag{16}$$

where $\mathcal{B}$ is the set of target blocks, $\mathbf{m}_b$ is the positional query of target block b, $\mathrm{sg}[\cdot]$ denotes stop-gradient through the target branch, and τ is the EMA momentum coefficient; the asymmetric context/target design with an EMA-updated target encoder follows the I-JEPA training construction [35].

Interpretation. The contrast between Eq. (15) and Eq. (16) is the experimental variable of this study. Eq. (15) places the residual in pixel space, so any high-frequency structure the encoder discards is paid for directly in the loss. Eq. (16) places the residual in a learned embedding space that is itself free to

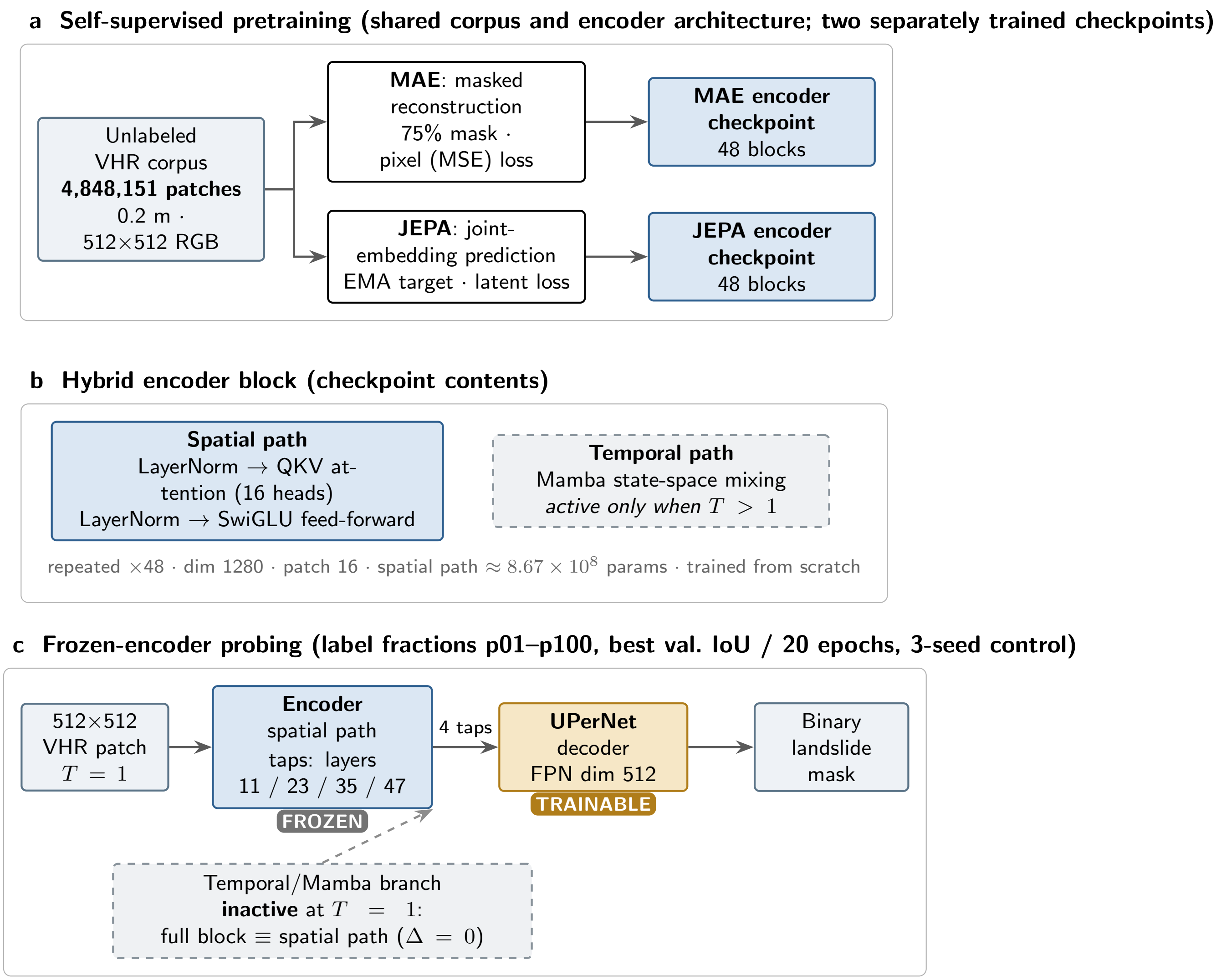

Figure 2: Architecture and evaluation protocol. The design isolates the self-supervised learning question: both objectives learn representations from the same large *unlabeled* VHR aerial corpus before any landslide labels are seen (panel a), so that downstream performance reflects the pretext objective rather than supervised adaptation. MAE and JEPA are trained from scratch on this shared corpus, producing two separate encoder checkpoints of identical architecture (panel a). Each self-supervised checkpoint contains hybrid spatial and temporal/state-space parameters; for single-frame downstream probes ($T = 1$) the block executes the spatial path only, and the temporal/Mamba branch (inactive, dashed) is excluded during checkpoint loading (panel b). Each encoder is then frozen and only a lightweight UPerNet decoder is trained on each label fraction (panel c); features from encoder layers 11, 23, 35, and 47 feed the decoder for binary landslide segmentation. Freezing the encoder holds downstream adaptation fixed, so differences between MAE and JEPA reflect differences between the pretrained representations produced by the two self-supervised recipes rather than label-driven fine-tuning. An equivalence test confirms zero numerical difference between the full block and the spatial path at $T = 1$.

become invariant to that structure, so detail that the target encoder does not represent is invisible to the objective. Section 5.1 argues that this difference governs the observed ordering on sparse, fine-grained geomorphic targets.

3.5 Frozen UPerNet probing and label-efficiency protocol

For each label fraction the pretrained encoder is frozen and only the UPerNet decoder (feature-pyramid dimension 512) is trained for binary landslide segmentation, with four intermediate feature maps extracted from layers 11, 23, 35, and 47. The supervised training set is partitioned into nested fractions p01, p05, p10, p25, p50, and p100, corresponding to 1–100% of training labels, all evaluated on the same validation set. Decoders are trained for 20 epochs of 500 steps using AdamW (learning rate 1×10^{-4}, weight decay 0.01) applied to the trainable decoder parameters only; the loss is a pixel-wise two-class cross-entropy with class weights of 1.0 (background) and 3.0 (landslide). Ground-truth masks are binarized at a pixel-value threshold of 128, predictions are taken as the argmax over the two-class logits, and all frozen-probe runs use a batch size of 2. Under this fixed update budget each probe run samples $20 \times 500 \times 2 = 20{,}000$ image instances, which is smaller than the full p100 pool (381,719 patches) and larger than the p01 pool; the protocol is therefore a fixed-compute label-pool comparison, in which the label fraction controls the pool from which supervision is drawn rather than the number of gradient updates, and all methods at a given fraction receive an identical budget. The best validation IoU over the 20 decoder-training epochs is reported, because final-epoch values can fluctuate under low-label training; final-epoch values are treated as diagnostic.

3.6 Evaluation metrics

We frame downstream probing as binary semantic segmentation and report foreground-class metrics computed from true-positive (TP), false-positive (FP), and false-negative (FN) landslide pixels at the operating threshold. Intersection over Union and the F1 score are defined as

$$\mathrm{IoU} = \frac{\mathrm{TP}}{\mathrm{TP} + \mathrm{FP} + \mathrm{FN}}, \qquad \mathrm{F1} = \frac{2\,\mathrm{TP}}{2\,\mathrm{TP} + \mathrm{FP} + \mathrm{FN}}, \tag{17}$$

with precision $= \mathrm{TP}/(\mathrm{TP} + \mathrm{FP})$ and recall $= \mathrm{TP}/(\mathrm{TP} + \mathrm{FN})$. IoU measures the overlap between predicted and reference landslide pixels, while F1 is the harmonic mean of precision and recall; both are computed on the landslide (foreground) class only. Overall pixel accuracy is not used as a primary metric because, under the benchmark's 4.86% positive-pixel fraction, it is dominated by the background class and can remain high even for detectors that recover little of the landslide foreground. Throughout, IoU on the landslide class is the primary reporting metric and F1 is reported alongside it.

3.7 Checkpoint policy and bias control

The primary MAE label-efficiency curve uses the pre-existing eff304k checkpoint, which was fixed before the downstream checkpoint sweep. A later eff310k checkpoint achieved the best p100 score in a post hoc local sweep, but because it was identified after downstream RER2023 probe evaluation it is reported only as a sensitivity analysis. This separation prevents the validation benchmark from being used both to select and to report the main checkpoint. A checkpoint-window analysis (eff294k–eff374k) and the multiseed study below quantify robustness.

3.8 Multiseed decoder-variance protocol

To quantify probe variance, the primary MAE checkpoint and the JEPA checkpoint were each evaluated with three decoder seeds at p01 and p100, holding the encoder checkpoint, data split, decoder architecture, epoch budget, and steps per epoch fixed and varying only decoder initialization and training randomness. Results are summarized as mean $\pm$ standard deviation of the best validation IoU and F1. This experiment quantifies decoder-probe seed variance — robustness of the comparison to decoder initialization and probe-training randomness — not the variance of the self-supervised pretraining itself, which would require independently repeated MAE and JEPA pretraining runs and is beyond the present compute budget.

3.9 Control experiments

Two controls test alternative explanations of the main result; both are evaluated at p100, the condition most favourable to the alternative hypotheses because the decoder receives its maximum amount of supervised training data. First, a randomly initialized, frozen encoder of identical architecture is probed with the same UPerNet decoder and training schedule using three decoder seeds; this measures how much performance the trainable decoder can achieve without pretrained representations. Second, a final-layer-only feature-tap ablation probes the primary MAE checkpoint using only the layer-47 feature map, replicated to all four decoder inputs so that the decoder architecture is unchanged; this tests whether the multi-level taps at layers 11, 23, 35, and 47 contribute beyond the deepest representation alone. Both controls use the same p100 split and probing protocol as the main experiments.

3.10 Supervised reference

A SegFormer-B2 model [49] is reported as a deliberately strong external-data supervised reference. It is initialized from the publicly available `nvidia/segformer-b2-finetuned-ade-512-512` checkpoint, i.e. a SegFormer-B2 already fine-tuned for ADE20k semantic segmentation; for our two-class landslide task the segmentation head is resized and re-initialized, while the pretrained encoder and its semantic-segmentation representation supply a strong external supervised prior. The model is then fine-tuned end to end on the same label fractions. This reference is not protocol-matched to the frozen probes and differs from the MAE and JEPA models in three respects simultaneously: it is supervised rather than self-supervised, externally pretrained on a large labeled semantic-segmentation corpus rather than trained from scratch on the in-domain aerial corpus, and fully fine-tuned rather than frozen. It therefore indicates an achievable performance level under external-data supervised transfer and is not a like-for-like representation-quality comparison with MAE or JEPA; we are comparing MAE and JEPA as matched

Table 2: Implementation and reproducibility details.

Component	Setting
Pretraining corpus	4,848,151 unlabeled RGB VHR patches (2,033 WebDataset shards)
Patch size / resolution	512×512 px, 0.2 m
Encoder depth / dim / heads / patch	48 / 1280 / 16 / 16
Encoder parameters (spatial path)	$\approx 8.67 \times 10^8$
MAE mask ratio / decoder depth	75% / 8 layers
JEPA target encoder	exponential moving average
Downstream decoder	UPerNet, feature-pyramid dim 512
Feature taps	encoder layers 11, 23, 35, 47
Label fractions	p01, p05, p10, p25, p50, p100
Decoder training	20 epochs $\times$ 500 steps
Batch size	2 (all frozen-probe runs)
Learning rate / weight decay	1×10^{-4} / 0.01
Loss	pixel-wise cross-entropy, class weights 1.0 (background) / 3.0 (landslide)
Optimizer	AdamW (decoder parameters only)
Metric selection	best validation IoU; final epoch diagnostic only
Hardware	1 $\times$ NVIDIA H100 80 GB GPU per probe run, bf16 mixed precision

self-supervised objectives, with SegFormer-B2 as a strong supervised external-data reference rather than as an equal SSL baseline.

To enable a fair comparison between in-domain self-supervised representations and external supervised pretraining, we additionally evaluate SegFormer-B2 under a *matched* frozen-encoder protocol. Here the ADE20k-pretrained SegFormer-B2 encoder is frozen and only the segmentation head is trained, using the same hyperparameters as the MAE and JEPA frozen probes (batch size 2, learning rate 1×10^{-4}, 20 epochs of 500 steps), on the same RER2023 label-efficiency splits and validation set, with the best validation IoU used for reporting. We verified that the encoder was fully frozen: the number of trainable encoder parameters was zero, while the trainable head contained 3.15M parameters. A sensitivity run with batch size 8 and learning rate 6×10^{-5} produced a similar saturation pattern with marginally higher values, confirming the qualitative conclusion is robust to this choice. This frozen SegFormer-B2 condition is a freeze-policy- and training-budget-aligned external supervised reference: the freeze policy, optimizer, schedule, label pools, and validation set match the SSL probes, while encoder architecture, parameter count, native feature hierarchy, and decoder head necessarily differ, so the comparison aligns training protocol rather than isolating the source of pretraining alone. The fully fine-tuned SegFormer-B2 above is reported as a strong externally pretrained, end-to-end fine-tuned reference rather than as an upper bound.

Table 3: Main label-efficiency results (validation IoU, landslide class). MAE, JEPA, and frozen SegFormer-B2 are frozen-encoder probes under an aligned freeze policy and training budget (head trained only); frozen SegFormer-B2 is comparable to MAE at p01 but plateaus under the tested budget while MAE improves with larger label pools up to p50 before levelling off. The eff310k row is a post hoc checkpoint-sensitivity analysis. The fine-tuned SegFormer-B2 row is a strong externally pretrained, end-to-end fine-tuned reference (ADE20k-pretrained), not a frozen-probe comparator.

Method / role	p01	p05	p10	p25	p50	p100
Frozen-encoder probes (aligned freeze policy and budget)						
MAE primary	0.3541	0.4053	0.4344	0.4419	0.4510	0.4480
JEPA	0.2931	0.3571	0.3677	0.3899	0.3927	0.3907
SegFormer-B2 (frozen enc.)	0.3515	0.3670	0.3716	0.3739	0.3795	0.3771
Checkpoint sensitivity (post hoc; not primary)						
MAE eff310k	0.3633	0.3650	0.3733	0.4397	0.4545	0.4464
Externally pretrained, end-to-end fine-tuned reference						
SegFormer-B2 (fine-tuned)	0.4338	0.4694	0.4881	0.5058	0.5219	0.5115

4 Results

4.1 MAE outperforms JEPA across label fractions

MAE outperforms JEPA at every label fraction under the matched frozen-probe protocol (Table 3; Figure 3). At p01, MAE reaches 0.3541 IoU compared with 0.2931 for JEPA; at p100, MAE reaches 0.4480 compared with 0.3907. The advantage persists across all intermediate fractions, with margins of 0.048–0.067 IoU, and the two curves separate immediately and do not converge as supervision increases. Masked reconstruction therefore provides stronger in-domain VHR landslide representations than JEPA-style feature prediction under the tested protocol, and the gap is a property of the representations rather than a transient low-label effect. All probes are trained under a fixed budget of $20{,}000$ sampled instances (Section 3.5); the small decrease from p50 to p100 for several encoders (e.g., MAE $0.4510 \rightarrow 0.4480$) reflects that at large label pools this fixed budget samples a shrinking fraction of the available data, and the difference is within decoder-seed variance (± 0.0075) rather than a genuine reversal.

4.2 The MAE–JEPA gap exceeds decoder-probe seed variance

Three-seed repeats confirm that the separation is not an artefact of a single decoder initialization (Table 4; Figure 4). At p01, MAE obtains 0.3586 ± 0.0042 IoU against 0.2940 ± 0.0021 for JEPA; at p100, MAE obtains 0.4515 ± 0.0075 against 0.4045 ± 0.0034. The MAE–JEPA differences — 0.0646 IoU at p01 and 0.0470 at p100 — exceed the measured decoder-seed standard deviations by roughly fifteenfold at p01 and sixfold at p100, and the same ordering holds for F1. The multiseed means also broadly track the single-seed primary curve. For MAE the two agree within one standard deviation (0.3541 versus 0.3586 ± 0.0042 at p01; 0.4480 versus 0.4515 ± 0.0075 at p100). For JEPA at p100 the single-seed primary value (0.3907) sits below the three-seed mean (0.4045 ± 0.0034) by more than the corresponding

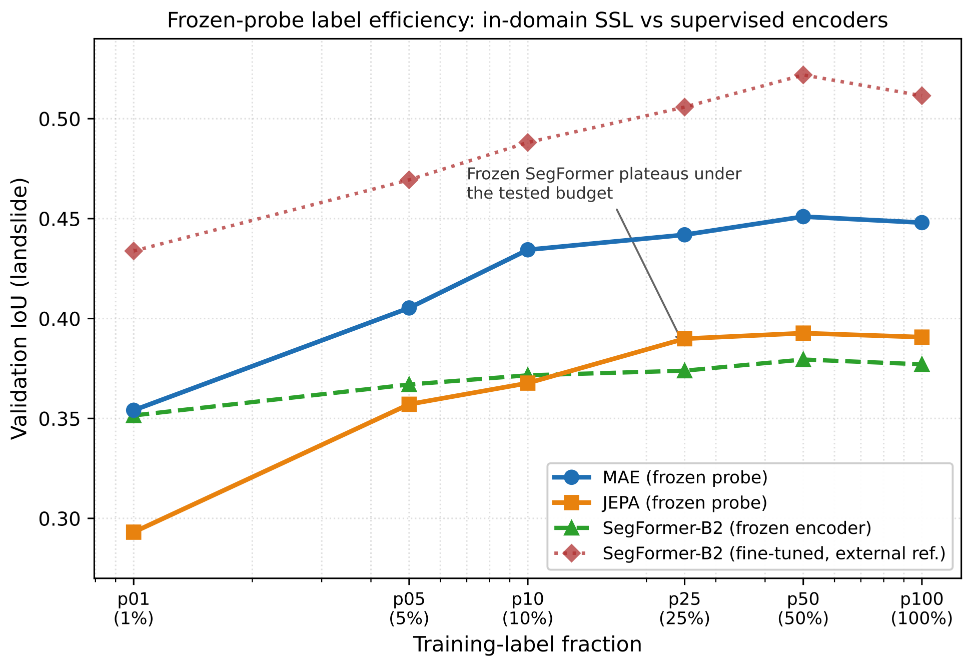

Figure 3: Label-efficiency comparison under frozen-probe and supervised fine-tuning protocols (validation IoU, landslide class). MAE and JEPA are frozen encoders pretrained with self-supervised objectives on in-domain VHR imagery and evaluated with the same UPerNet probe. Frozen SegFormer-B2 is an ADE20k-supervised encoder evaluated under a matched frozen-encoder setting (head trained only); under this head architecture and fixed training budget it is comparable to MAE at p01 but plateaus near 0.37–0.38 IoU, while MAE improves with larger label pools through p50 (levelling off marginally at p100) and surpasses it from p05 onward. JEPA remains below MAE throughout and is broadly comparable to frozen SegFormer-B2 at the higher fractions. Fully fine-tuned SegFormer-B2 is shown as a strong externally pretrained, end-to-end fine-tuned reference and is not a frozen-probe comparator.

Table 4: Three-seed frozen-probe results (mean $\pm$ SD of best validation IoU and F1).

Method	Fraction	IoU	F1
JEPA	p01	0.2940 ± 0.0021	0.4544 ± 0.0026
MAE	p01	0.3586 ± 0.0042	0.5279 ± 0.0045
JEPA	p100	0.4045 ± 0.0034	0.5759 ± 0.0035
MAE	p100	0.4515 ± 0.0075	0.6221 ± 0.0070

MAE offset; because the primary label-efficiency curves are single-seed runs and the three-seed study varies only decoder initialization and training randomness, we treat the three-seed means as the more reliable point estimates and report the single-seed curves for the full fraction sweep. The single-seed JEPA and MAE primary runs share the same probe configuration (identical decoder architecture, label split, epoch budget, and steps per epoch), so this offset reflects decoder-probe randomness rather than a protocol difference between the two methods. We emphasize that this experiment quantifies robustness to decoder-probe randomness under fixed pretrained checkpoints; it does not measure the run-to-run variance of the self-supervised pretraining itself.

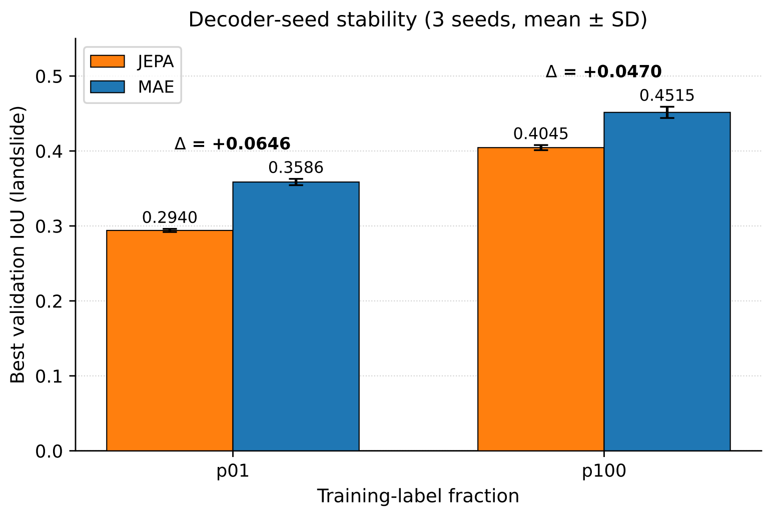

Figure 4: Decoder-probe seed stability. Three decoder seeds at p01 and p100 (mean $\pm$ SD), with encoder checkpoints held fixed, show that MAE remains stronger than JEPA and that the gap exceeds decoder-probe seed variance by roughly fifteenfold at p01 and sixfold at p100.

4.3 Checkpoint sensitivity and fine-tuning diagnostics

Downstream transfer is sensitive to the pretraining checkpoint (Figure 5). Within the dedicated checkpoint-window sweep, eff310k gave the highest p100 result under that sweep's probe runs (0.4464 versus 0.4429 for eff304k), while the primary-curve p100 value for eff304k (0.4480, Table 3) remains the highest reported p100 number; eff310k improves some fractions while degrading others relative to the primary curve (e.g., -0.061 IoU at p10, $+0.004$ at p50); because it was identified after downstream validation, it is reported only as sensitivity. Continued pretraining to eff374k degraded downstream transfer, indicating that reconstruction loss alone is not a sufficient checkpoint selector. Staged full fine-tuning with layer-wise learning-rate decay stabilized training that otherwise collapsed, but did not outperform the frozen primary curve (IoU approximately 0.3589, 0.3578, 0.3790, and 0.3662 at p01, p05, p10, and p100, respectively). For this corpus and architecture, the pretrained representation is most useful when the encoder is kept fixed and only the decoder is trained — itself an informative result, indicating that the representation is already well structured for the task rather than serving merely as an initialization.

4.4 Comparison with generic pretraining and full fine-tuning

Two further comparisons isolate what the in-domain self-supervised pretraining contributes. First, to test whether generic pretrained visual features already explain the result, we probe a standard ImageNet-pretrained ViT-B/16 encoder (`augreg_in21k_ft_in1k`) with the same UPerNet decoder and protocol, feeding appropriate intermediate depths (layers 2, 5, 8, 11) to the decoder. We emphasize that this is not architecture-matched: ViT-B/16 is a substantially smaller and differently pretrained model (roughly 8.6×10^7 parameters versus the ChronoSat encoder's $\approx 8.67 \times 10^8$), so the comparison contrasts pretraining paradigms rather than isolating pretraining data alone. The ImageNet encoder is competitive

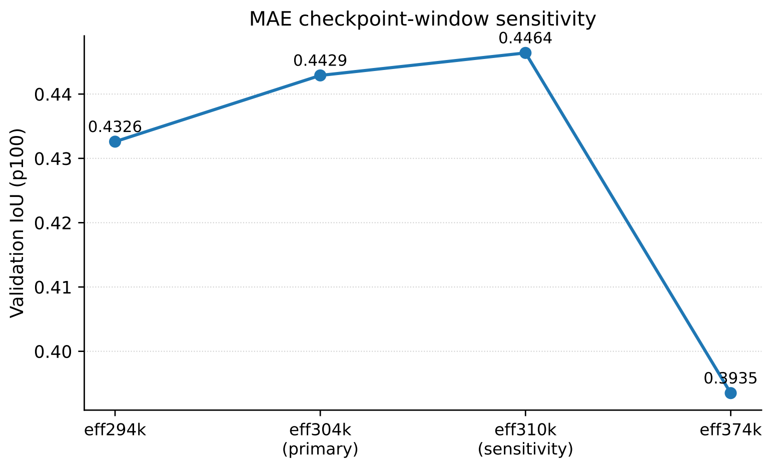

Figure 5: MAE checkpoint-window sensitivity (eff294k–eff374k). The eff310k checkpoint is disclosed as sensitivity rather than used as the primary result because it was selected after downstream probe evaluation; continued pretraining to eff374k degrades transfer. Sweep values come from dedicated decoder-training runs; their differences from the corresponding Table 3 entries (e.g., 0.4429 versus 0.4480 for eff304k at p100) are smaller than the measured decoder-seed standard deviation ($\pm$0.0075).

in the most label-scarce regime — it reaches 0.3763 IoU at p01, marginally above the primary MAE probe (0.3541) — but ChronoSat-MAE surpasses it as labels increase, at p10 (0.4344 versus 0.3985) and p100 (0.4480 versus 0.4075). Generic pretrained features thus provide a strong low-label prior, while in-domain self-supervised pretraining yields representations that scale more effectively with landslide supervision. The randomly initialized frozen encoder of identical architecture remains far below all pretrained encoders at p100 (0.1429 ± 0.0219 IoU across three decoder seeds; Table 5), the fraction most favourable to decoder learning, confirming that the trainable decoder alone does not account for the result.

Second, we tested whether unfreezing the encoder improves over frozen probing. The primary MAE result uses a frozen encoder with a trainable UPerNet decoder and reaches 0.4480 p100 validation IoU. In a staged full fine-tuning diagnostic with layer-wise learning-rate decay, the encoder was unfrozen and optimized at a lower learning rate; its best p100 validation IoU was 0.3662 (Section 4.3), with a lower final-epoch value, so full fine-tuning did not improve over the frozen-probe protocol in the tested configuration. The frozen-probe protocol therefore measures encoder representation quality directly, and all main MAE–JEPA comparisons are reported under it.

4.5 Control experiments

Both controls fall below the pretrained four-tap probes at p100 (Table 5; Figure 6). The randomly initialized frozen encoder reaches 0.1429 ± 0.0219 IoU (F1 0.2496 ± 0.0340) across three decoder seeds — less than a third of the MAE probe (0.4515 ± 0.0075) and far below JEPA (0.4045 ± 0.0034) — even though p100 provides the decoder with its maximum supervised training data. Decoder capacity alone therefore explains only a minor fraction of the observed performance, and the MAE–JEPA comparison

Table 5: Diagnostic controls and matched p100 frozen-probe references (validation IoU; mean $\pm$ SD over three decoder seeds where indicated). The random-encoder and tap-47 rows are diagnostic controls; the four-tap JEPA and MAE rows are matched reference probes.

Experiment	IoU (p100)
Random frozen encoder (3 seeds)	0.1429 ± 0.0219
MAE final-layer-only (tap 47)	0.3938
JEPA four-tap probe (3 seeds)	0.4045 ± 0.0034
MAE four-tap probe, primary checkpoint	0.4480
MAE four-tap probe (3 seeds)	0.4515 ± 0.0075

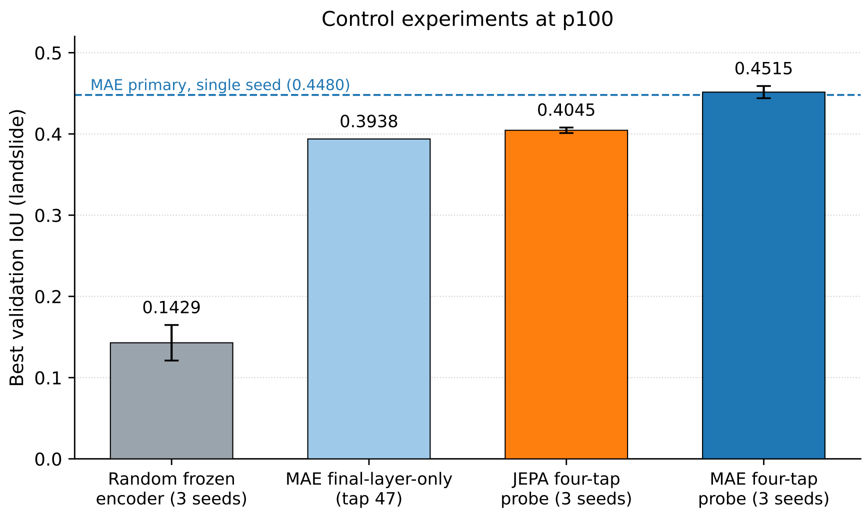

Figure 6: Diagnostic controls and matched p100 frozen-probe references. The randomly initialized frozen encoder (three decoder seeds) and the final-layer-only (tap-47) MAE probe are diagnostic controls; the four-tap JEPA and MAE probes are matched reference probes. The final-layer-only (tap-47) probe is a single decoder-seed run and therefore has no error bar; the randomly initialized and four-tap probes show mean $\pm$ SD over three decoder seeds. The dashed line marks the primary single-seed MAE result (0.4480 IoU).

measures pretrained representation quality rather than decoder learning. The final-layer-only ablation reaches 0.3938 IoU (F1 0.5651): the deepest representation alone recovers approximately 88% of the four-tap configuration (0.4480), while the multi-level taps contribute a further $+0.0542$ IoU. This gain is roughly seven times the decoder-seed standard deviation and is comparable in magnitude to the full MAE–JEPA separation at p100 (0.0470), so the probing protocol is not a cosmetic choice: single-layer probing would understate dense-segmentation performance by an amount similar to the inter-method gap itself.

4.6 Qualitative segmentation analysis

Qualitative examples illustrate the quantitative trends (Figure 7). Four illustrative validation patches were selected to span the range of relative outcomes — two MAE-favouring cases (a sparse and a moderate landslide), one case in which the two probes are comparable, and one JEPA-favouring case — and are therefore illustrative of outcome types rather than a random or statistically representative sample. Each method's prediction is rendered as a per-pixel error map relative to the ground truth, using a single consistent colour scheme (green: true positive; red: false positive; blue: false negative; yellow outline: ground-truth boundary). In the MAE-favouring cases, MAE produces localized, geomorphologically coherent detections while JEPA either misses the target or generates large false-positive regions over bare ground. These patterns are consistent with the higher p100 validation IoU observed quantitatively, while the JEPA-favouring case shows the ordering is not uniform at patch level. The failure modes shared by both probes are large or fragmented failures with substantial false-negative areas, reflecting the difficulty of small targets, ambiguous boundaries, and terrain or land-cover textures that resemble landslide surfaces.

5 Discussion

5.1 Why masked reconstruction is better aligned with VHR landslide morphology

The strongest result is not simply that MAE attains higher IoU than JEPA, but that the difference is systematic across label fractions and stable under repeated decoder training. VHR landslide segmentation depends on local morphology: scar boundaries, disturbed texture, debris patterns, vegetation discontinuities, road-cut failures, and channel-adjacent erosion. The landslide foreground is sparse (under 5% of pixels) and visually close to background surfaces such as bare soil, riverbeds, and disturbed agricultural land, so the diagnostic signal resides largely in high-frequency texture and boundary structure. One plausible explanation — which we advance as a hypothesis consistent with, but not directly demonstrated by, our experiments — is that MAE's pixel-space reconstruction objective compels the encoder to preserve precisely this detail, whereas JEPA's feature-space prediction objective is designed to discard low-level content in favour of higher-level invariances, an advantage demonstrated principally on classification probes and low-level tasks such as depth and counting, not on dense segmentation. Under this hypothesis, for sparse, fine-grained geomorphic targets the usual ranking of objectives inverts: the high-frequency information that feature prediction is built to suppress is the information a downstream segmenter needs, and the effect would be strongest in the low-label regime, where decoder training data are insufficient to relearn fine-scale cues that the representation does not already carry. Direct tests of this mechanism — boundary-quality metrics at pixel tolerances, landslide-size-stratified IoU, or representation-level frequency and similarity analyses — were not performed here and are a priority for follow-up work. We note that, although this mechanism makes the direction of the result interpretable in hindsight, it runs counter to the prevailing empirical picture: joint-embedding prediction was introduced and is frequently reported as matching or surpassing reconstruction-based pretraining on downstream evaluation, with its documented advantages concentrated on image classification under linear probing and on low-level tasks such as depth estimation and object counting. Demonstrating, under a controlled matched protocol, that this ordering reverses for dense VHR landslide segmentation is therefore an empirical contribution rather than a foregone conclusion. We also emphasize that our com-

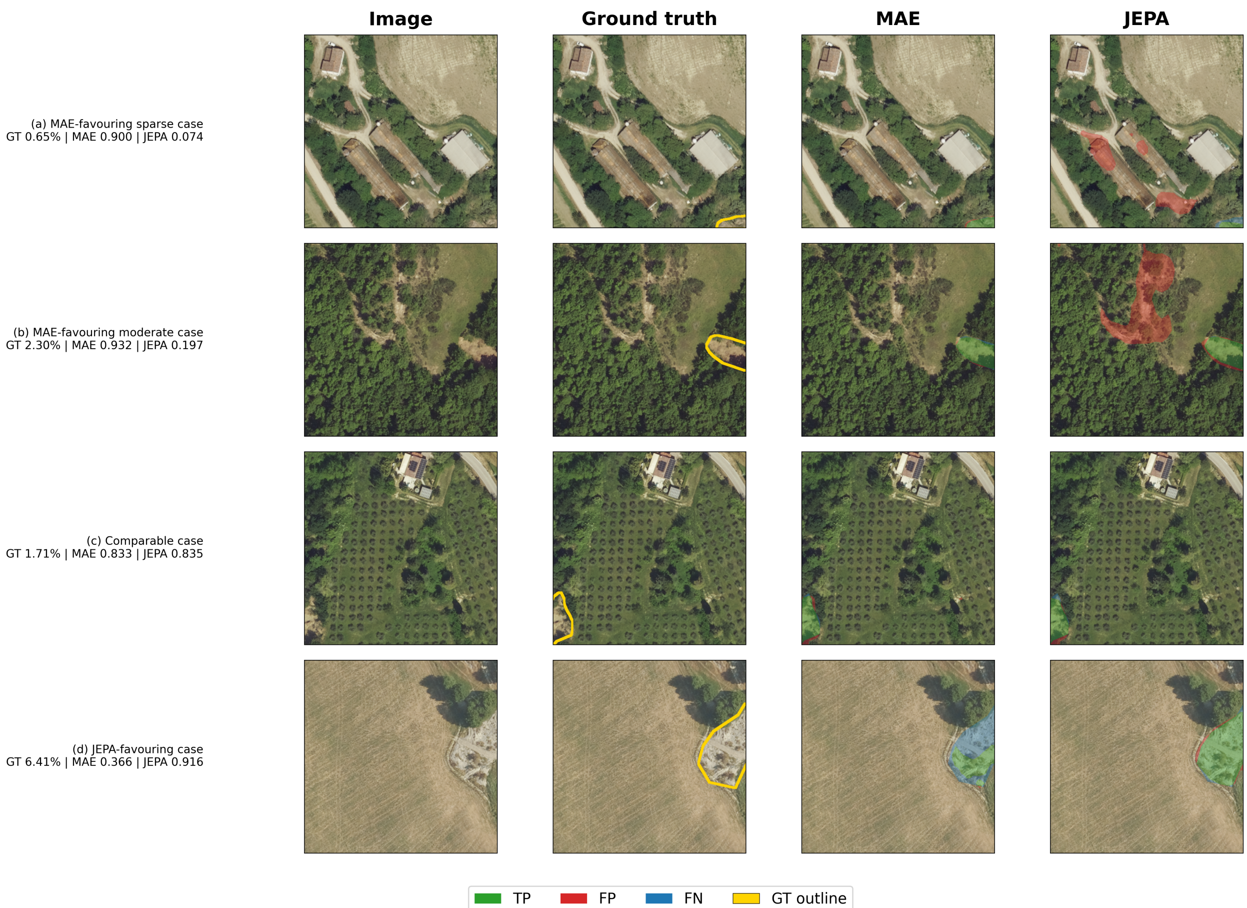

Figure 7: Qualitative comparison of frozen MAE and JEPA UPerNet probes on illustrative RER2023 validation patches, selected to span MAE-favouring, comparable, and JEPA-favouring outcomes (per-panel labels); they are illustrative cases, not a random sample. Per-panel numeric annotations report the landslide-class IoU for each method on that patch, and the GT value is the landslide fraction of the patch. A single consistent colour scheme is used throughout: the ground-truth landslide boundary is drawn as a yellow outline, and each method's prediction is rendered as a per-pixel error map relative to that ground truth, with green marking true positives, red marking false positives, and blue marking false negatives. Each colour therefore has one fixed meaning across all columns. The examples illustrate that MAE generally provides more localized and geomorphologically coherent predictions (larger green, smaller red and blue regions) than JEPA, while both methods remain challenged by small targets, ambiguous boundaries, and complex terrain or land-cover conditions.

parison uses the standard JEPA objective without segmentation-specific modification; a JEPA variant explicitly adapted for boundary-sensitive dense prediction (for example, with higher-resolution targets or an auxiliary reconstruction term) might narrow or close the gap, and testing such variants is a natural and worthwhile direction for future work. The present finding should accordingly be read as a statement about the two objectives in their standard forms under a matched frozen-probe protocol, not as a claim that feature-space prediction is inherently unsuited to segmentation.

5.2 Why the supervised reference remains higher

The matched frozen-encoder comparison clarifies the role of external supervised pretraining versus in-domain self-supervised representation learning. A frozen SegFormer-B2 encoder pretrained on ADE20k supplies strong generic visual features in the extreme low-label regime, comparable to MAE at the smallest fraction (0.3515 versus 0.3541 IoU at p01). However, under this head architecture and training budget its frozen features plateau, rising only to 0.3771 IoU at p100 despite the increase in head supervision. The in-domain MAE representation instead improves substantially as more landslide labels become available, increasing from 0.3541 at p01 to 0.4510 at p50, and is already clearly ahead of the frozen supervised encoder from p05 onward. This crossover indicates that the externally supervised encoder provides useful generic semantic features, but that these features are less aligned with landslide morphology and VHR aerial-image structure than the MAE representation learned directly from the target regional imagery; the in-domain representation has more landslide-relevant signal for the probe to extract as supervision increases. JEPA remains below MAE across the entire curve and is broadly comparable to, and at the highest fractions marginally above, the frozen SegFormer-B2 baseline (e.g. 0.3907 versus 0.3771 at p100). The fully fine-tuned SegFormer-B2 remains higher than all frozen encoders at every fraction and is reported as a strong externally pretrained, end-to-end fine-tuned reference, not a frozen-probe comparator; its strong low-label performance reflects transfer from millions of external labeled images rather than landslide-label efficiency. These results support a nuanced conclusion: in-domain MAE does not simply dominate supervised external pretraining in every regime, but under matched frozen-probe conditions it matches a strong supervised encoder at the smallest fraction and scales better with label availability, clearly surpassing it as labels increase, while consistently exceeding JEPA.

5.3 The role of multi-level feature taps

The final-layer-only control refines, rather than merely confirms, the role of multi-level probing. We use *multi-level* deliberately: all four taps share the same $32 \times 32 \times 1280$ token geometry and differ in encoder depth, unlike the natively hierarchical multiscale features of, e.g., SegFormer. Using only the deepest tap lowers p100 IoU from 0.4480 to 0.3938 (-0.0542), indicating that layer 47 carries most, but not all, of the task-relevant signal. The four-tap configuration nevertheless adds $+0.0542$ IoU — roughly seven times the decoder-seed standard deviation and comparable to the entire MAE–JEPA separation at the same fraction — with shallower taps plausibly contributing the boundary-scale detail that the deepest layer has abstracted away. Two methodological consequences follow. First, multi-level probing is the appropriate protocol for evaluating representations for dense geoscientific prediction, because single-layer probes understate achievable performance by an amount similar to typical inter-method differences. Second, probing protocol and pretraining objective must be varied one at a time: the single-tap MAE probe (0.3938) falls below the four-tap JEPA probe (0.4045), so an uncontrolled comparison that mixed protocols could invert the apparent method ranking. The matched four-tap protocol used throughout this study is what licenses the MAE–JEPA conclusion.

5.4 Limits of regional, RGB-only, single-frame representation learning

The results should not be generalized beyond the evidence. The pretraining corpus is regional and RGB-only; it contains no DEM, SAR, multispectral, thermal, or explicit time-series information. The downstream task is single-frame segmentation, so the temporal/state-space branch of the hybrid checkpoint is inactive at $T = 1$, and the reported probes characterize the spatial pathway of the pretrained encoder — verified to be numerically identical to the full block under single-frame execution. Cross-domain behaviour was not the focus of this study and should be treated as an open question rather than a demonstrated strength. Future work should test multi-region transfer, DEM/SAR/multispectral fusion, acquisition-year robustness, landslide-trigger differences, multi-temporal probing in which the state-space pathway activates, and the influence of spatial autocorrelation between training and validation areas.

5.5 Limitations

The main limitations are fourfold. First, the evaluation is in-domain and potentially transductive: the pretraining corpus and downstream benchmark share the same regional footprint, and the 2023 pretraining epoch is contemporaneous with the labeled benchmark, so unlabeled pretraining imagery may spatially overlap validation geography. Labels were never supplied during pretraining, but a quantitative spatial-overlap audit between the unlabeled corpus and the validation tiles, and a pretraining ablation excluding the 2023 epoch or the validation geography, are required before the comparison against externally pretrained encoders can be read as fully leakage-free; both are planned for the revised release. Second, the imagery is RGB-only, excluding modalities known to aid landslide mapping. Third, the downstream probe is single-frame, so conclusions concern the spatial pathway of the encoder; multi-temporal behaviour is untested. Fourth, the segmentation benchmark, although large, derives from a single regional inventory and triggering event, so inventory-specific mapping conventions may influence absolute scores. We do not claim a general Earth-observation foundation model; the study should be read as evidence for domain-specialized, label-efficient VHR landslide representation learning.

5.6 Implications for geoscience machine learning

For geoscience machine learning, the principal implication is practical: when the target process carries fine morphological structure, as VHR landslides do, the choice of self-supervised objective directly affects how efficiently scarce expert labels can be converted into accurate maps. Pixel reconstruction — often considered the less semantic objective — appears to be the better foundation here, consistent with its retention of the decimetric boundary and texture detail that distinguishes landslide scars from the bare soil, riverbeds, and disturbed ground that mimic them. For hazard mapping under realistic conditions, where unlabeled VHR archives are abundant but expert annotation is the binding constraint, this favours building domain-specific landslide encoders on masked reconstruction rather than importing feature-prediction objectives transferred from satellite-resolution or natural-image settings. The result also carries a methodological caution: the apparent ranking of self-supervised objectives can be reversed by the downstream protocol, so claims about which objective is "better" for Earth observation should be evaluated on the target task and resolution rather than inherited from classification benchmarks. Checkpoint-selection policy, multiseed probing, frozen-versus-fine-tuning diagnostics, randomized-encoder and feature-tap controls, and architecture-path verification each closed an alternative explanation, together converting a leaderboard-style comparison into a representation-learning finding.

6 Conclusion

We compared MAE and JEPA for self-supervised VHR landslide representation learning under a matched frozen-encoder UPerNet protocol on a 449,153-pair regional benchmark. MAE outperformed JEPA across all six label fractions, the gap exceeded decoder-probe seed variance by roughly an order of magnitude at p01 and about sixfold at p100, and control experiments showed that decoder capacity alone recovers less than a third of the observed performance while multi-level feature taps contribute a gain comparable to the MAE–JEPA separation itself. Checkpoint-sensitivity and fine-tuning diagnostics support a conservative interpretation: MAE provides stronger in-domain frozen representations than JEPA. A freeze-policy- and budget-aligned comparison further shows that a strong ADE20k-supervised SegFormer-B2 encoder is comparable to MAE only at the smallest label fraction before its frozen features plateau under the tested budget, whereas MAE improves with larger label pools through p50 and clearly surpasses it from p05 onward; an end-to-end fine-tuned SegFormer-B2, reported as a strong externally pretrained reference, remains higher. An architecture audit confirms that single-frame probing follows the spatial pathway of the hybrid pretrained encoder exactly as defined by its $T = 1$ execution path. Overall, masked reconstruction is better aligned than feature-space prediction with VHR landslide morphology, supporting reconstruction-based self-supervision for domain-specialized, label-efficient geoscience segmentation.

Data availability

The supervised landslide benchmark comprises 449,153 image–mask pairs derived from the publicly available 2023 Emilia-Romagna landslide inventory [45]; the unlabeled VHR pretraining corpus is derived from the same regional aerial imagery. The processed image–mask patches, the unlabeled pretraining corpus, and the exact train and validation split files will be deposited in a public repository with a persistent identifier upon acceptance.

Code availability

Pretraining, frozen-probing, control-experiment, and figure-generation code, together with the primary model checkpoints, will be deposited in the same public repository upon acceptance.

Acknowledgments

S.R.M. acknowledges support from the NATURA project, funded by the Italian Ministry of University and Research (MUR) under the FIS3 (Fondo Italiano per la Scienza) Starting Grant programme (grant FIS-2024-07495), and institutional support from OGS (Istituto Nazionale di Oceanografia e di Geofisica Sperimentale), Trieste. This work was also supported by the Sichuan Science and Technology Program (No.2026NSFSC0439, 2024ZDZX0020); the Opening fund of State Key Laboratory of Geohazard Prevention and Geoenvironment Protection (Chengdu University of Technology) (No. SKLGP2025K025); and the Academic Degree and Postgraduate Education Reform Project of Sichuan Province (No. YJGXM24-C036). The authors thank the regional data providers and acknowledge the University of Padua DGX computing facility supporting this work.

Author contributions

S.R.M. conceived the study, developed the methodology and software, conducted the investigation and data curation, performed the formal analysis and visualization, wrote the original draft, and prepared the manuscript. X.T. and F.C. reviewed the manuscript and provided comments. All authors read and approved the submitted version.

Competing interests

The authors declare no competing interests.

References

[1] Melanie J. Froude and David N. Petley. Global fatal landslide occurrence from 2004 to 2016. *Natural Hazards and Earth System Sciences*, 18:2161–2181, 2018. doi: 10.5194/nhess-18-2161-2018.

[2] Fausto Guzzetti, Alessandro C. Mondini, Mauro Cardinali, Federica Fiorucci, Michele Santangelo, and Kang-Tsung Chang. Landslide inventory maps: New tools for an old problem. *Earth-Science Reviews*, 112(1–2):42–66, 2012. doi: 10.1016/j.earscirev.2012.02.001.

[3] Tapas R. Martha, Norman Kerle, Victor Jetten, Cees J. van Westen, and K. Vinod Kumar. Characterising spectral, spatial and morphometric properties of landslides for semi-automatic detection using object-oriented methods. *Geomorphology*, 116(1):24–36, 2010. doi: 10.1016/j.geomorph.2009.10.004.

[4] André Stumpf and Norman Kerle. Object-oriented mapping of landslides using Random Forests. *Remote Sensing of Environment*, 115(10):2564–2577, 2011. doi: 10.1016/j.rse.2011.05.013.

[5] Omid Ghorbanzadeh, Thomas Blaschke, Khalil Gholamnia, Sansar Raj Meena, Dirk Tiede, and Jagannath Aryal. Evaluation of different machine learning methods and deep-learning convolutional neural networks for landslide detection. *Remote Sensing*, 11(2):196, 2019. doi: 10.3390/rs11020196.

[6] Sansar Raj Meena, Lucas Pedrosa Soares, Carlos H. Grohmann, Cees van Westen, Kushanav Bhuyan, Ramesh P. Singh, et al. Landslide detection in the Himalayas using machine learning algorithms and U-Net. *Landslides*, 19(5):1209–1229, 2022. doi: 10.1007/s10346-022-01861-3.

[7] Shunping Ji, Dawen Yu, Chaoyong Shen, Weile Li, and Qiang Xu. Landslide detection from an open satellite imagery and digital elevation model dataset using attention boosted convolutional neural networks. *Landslides*, 17(6):1337–1352, 2020. doi: 10.1007/s10346-020-01353-2.

[8] Xiaochuan Tang, Zhihua Tu, Yi Wang, Ming Liu, Dongfen Li, and Xuanmei Fan. Automatic detection of coseismic landslides using a new transformer method. *Remote Sensing*, 14(12):2884, 2022. doi: 10.3390/rs14122884.

[9] Zijin Fu, Fawu Wang, Junfei Zhong, Filippo Catani, Jie Dou, Qi You, and Bo Zhang. A CNN–Transformer hybrid network for efficient cross-region landslide detection by transfer learning. *Landslides*, 2026. doi: 10.1007/s10346-026-02733-w.

[10] Xiaochuan Tang, Zhong Lu, Xuanmei Fan, Xiaochuang Yan, Xiaojun Yuan, Dongfen Li, et al. Mamba for landslide detection: A lightweight model for mapping landslides with very high-resolution images. *IEEE Transactions on Geoscience and Remote Sensing*, 63:5637117, 2025. doi: 10.1109/TGRS.2025.3598446.

[11] Chengyong Fang, Xuanmei Fan, Xin Wang, Kushanav Bhuyan, Hao Zhong, Xiangyang Dou, Mingyao Xia, and Filippo Catani. Rapid and robust landslide mapping from optical EO imagery using a Mamba-based deep learning framework. *Landslides*, 2026. doi: 10.1007/s10346-026-02789-8.

[12] Penglei Li, Yi Wang, Tongzhen Si, Kashif Ullah, Wei Han, and Lizhe Wang. MFFSP: Multi-scale feature fusion scene parsing network for landslides detection based on high-resolution satellite images. *Engineering Applications of Artificial Intelligence*, 127:107337, 2024. doi: 10.1016/j.engappai.2023.107337.

[13] Wenqi Lu, Yu Hu, Zhe Zhang, and Wei Cao. A dual-encoder U-Net for landslide detection using Sentinel-2 and DEM data. *Landslides*, 2023. doi: 10.1007/s10346-023-02089-5.

[14] Aimin Dong, Jie Dou, Chao Li, Zhu Chen, Jiahao Ji, Kaiming Xing, et al. Accelerating cross-scene co-seismic landslide detection through progressive transfer learning and lightweight deep learning strategies. *IEEE Transactions on Geoscience and Remote Sensing*, 62:1–13, 2024. doi: 10.1109/TGRS.2024.3424680.

[15] Omid Ghorbanzadeh, Yonghao Xu, Pedram Ghamisi, Michael Kopp, and David Kreil. Landslide4Sense: Reference benchmark data and deep learning models for landslide detection. *IEEE*

Transactions on Geoscience and Remote Sensing, 60:1–17, 2022. doi: 10.1109/TGRS.2022.3215209.

[16] Lorenzo Nava, Alessandro Mondini, Kushanav Bhuyan, Chengyong Fang, Oriol Monserrat, Alessandro Novellino, and Filippo Catani. Sentinel-1 SAR-based globally distributed co-seismic landslide detection by deep neural networks. *Geoscientific Model Development*, 19:167–185, 2026. doi: 10.5194/gmd-19-167-2026.

[17] Xiaochuan Tang et al. FMLD: A vertical federated learning framework for privacy-preserving multimodal landslide detection. *Journal of Geophysical Research: Machine Learning and Computation*, 3:e2025JH000857, 2026. doi: 10.1029/2025JH000857.

[18] Jia Deng, Wei Dong, Richard Socher, Li-Jia Li, Kai Li, and Li Fei-Fei. ImageNet: A large-scale hierarchical image database. In *2009 IEEE Conference on Computer Vision and Pattern Recognition*, pages 248–255, 2009. doi: 10.1109/CVPR.2009.5206848.

[19] Filippo Catani. Landslide detection by deep learning of non-nadiral and crowdsourced optical images. *Landslides*, 18(3):1025–1044, 2021. doi: 10.1007/s10346-020-01513-4.

[20] Sansar Raj Meena, Lorenzo Nava, Kushanav Bhuyan, Silvia Puliero, Lucas Pedrosa Soares, Helen C. Dias, et al. HR-GLDD: a globally distributed dataset using generalized deep learning (DL) for rapid landslide mapping on high-resolution (HR) satellite imagery. *Earth System Science Data*, 15(7): 3283–3298, 2023. doi: 10.5194/essd-15-3283-2023.

[21] Yulin Xu, Chaojun Ouyang, Qiang Xu, Dongpo Wang, Bo Zhao, and Yuntao Luo. CAS Landslide Dataset: A large-scale and multisensor dataset for deep learning-based landslide detection. *Scientific Data*, 11(1):12, 2024. doi: 10.1038/s41597-023-02847-z.

[22] Chengyong Fang, Xuanmei Fan, Xin Wang, Lorenzo Nava, Hao Zhong, Xiujun Dong, Jixiao Qi, and Filippo Catani. A globally distributed dataset of coseismic landslide mapping via multi-source high-resolution remote sensing images. *Earth System Science Data*, 16:4817–4842, 2024. doi: 10.5194/essd-16-4817-2024.

[23] Guanting Liu, Yi Wang, Xi Chen, Baoyu Du, Penglei Li, Yuan Wu, Zhice Fang, and Peifeng Ma. LMHLD: A large-scale multisource high-resolution landslide dataset for landslide detection based on deep learning. *IEEE Transactions on Geoscience and Remote Sensing*, 63:1–15, 2025. doi: 10.1109/TGRS.2025.3619062.

[24] Kushanav Bhuyan, Hakan Tanyạş, Lorenzo Nava, Silvia Puliero, Sansar Raj Meena, Mario Floris, et al. Generating multi-temporal landslide inventories through a general deep transfer learning strategy using HR EO data. *Scientific Reports*, 13(1):162, 2023. doi: 10.1038/s41598-022-27352-y.

[25] Lei Wu, Ruixin Liu, Nengpan Ju, Ailin Zhang, Jinsong Gou, Guangle He, and Yixin Lei. Landslide mapping based on a hybrid CNN-transformer network and deep transfer learning using remote

sensing images with topographic and spectral features. *International Journal of Applied Earth Observation and Geoinformation*, 126:103612, 2024. doi: 10.1016/j.jag.2023.103612.

[26] Zijin Fu, Fawu Wang, Zihan Tu, Xingliang Peng, Gang Liu, and Filippo Catani. LSDSAM: Harnessing visual foundation model and enhanced transfer learning toward practical landslide detection in few-shot scenarios. *IEEE Journal of Selected Topics in Applied Earth Observations and Remote Sensing*, 19:12344–12365, 2026. doi: 10.1109/JSTARS.2026.3678141.

[27] Chao Yang, Yi Zhu, Jin Zhang, Xin Wei, Hong Zhu, and Zhe Zhu. A feature fusion method on landslide identification in remote sensing with Segment Anything Model. *Landslides*, 22(2):471–483, 2025. doi: 10.1007/s10346-024-02390-x.

[28] Jie Yu, Yi Li, Yang Chen, Chao Hou, Daqing Ge, Yan Ma, and Qiang Wu. LandslideNet: Adaptive vision foundation model for landslide detection. In *IGARSS 2024 – IEEE International Geoscience and Remote Sensing Symposium*, pages 7282–7285, 2024. doi: 10.1109/IGARSS53475.2024.10641507.

[29] Kaiming He, Xinlei Chen, Saining Xie, Yanghao Li, Piotr Dollár, and Ross Girshick. Masked autoencoders are scalable vision learners. In *Proceedings of the IEEE/CVF Conference on Computer Vision and Pattern Recognition*, pages 16000–16009, 2022.

[30] Zhenda Xie, Zheng Zhang, Yue Cao, Yutong Lin, Jianmin Bao, Zhuliang Yao, Qi Dai, and Han Hu. SimMIM: A simple framework for masked image modeling. In *Proceedings of the IEEE/CVF Conference on Computer Vision and Pattern Recognition*, pages 9643–9653, 2022.

[31] Hangbo Bao, Li Dong, Songhao Piao, and Furu Wei. BEiT: BERT pre-training of image transformers. In *International Conference on Learning Representations (ICLR)*, 2022.

[32] Alexey Dosovitskiy, Lucas Beyer, Alexander Kolesnikov, Dirk Weissenborn, Xiaohua Zhai, Thomas Unterthiner, Mostafa Dehghani, Matthias Minderer, Georg Heigold, Sylvain Gelly, Jakob Uszkoreit, and Neil Houlsby. An image is worth 16x16 words: Transformers for image recognition at scale. In *International Conference on Learning Representations (ICLR)*, 2021.

[33] Kaiming He, Haoqi Fan, Yuxin Wu, Saining Xie, and Ross Girshick. Momentum contrast for unsupervised visual representation learning. In *Proceedings of the IEEE/CVF Conference on Computer Vision and Pattern Recognition*, pages 9729–9738, 2020.

[34] Ting Chen, Simon Kornblith, Mohammad Norouzi, and Geoffrey Hinton. A simple framework for contrastive learning of visual representations. In *Proceedings of the 37th International Conference on Machine Learning (ICML)*, pages 1597–1607, 2020.

[35] Mahmoud Assran, Quentin Duval, Ishan Misra, Piotr Bojanowski, Pascal Vincent, Michael Rabbat, Yann LeCun, and Nicolas Ballas. Self-supervised learning from images with a joint-embedding predictive architecture. In *Proceedings of the IEEE/CVF Conference on Computer Vision and Pattern Recognition*, pages 15619–15629, 2023.

[36] Mathilde Caron, Hugo Touvron, Ishan Misra, Hervé Jégou, Julien Mairal, Piotr Bojanowski, and Armand Joulin. Emerging properties in self-supervised vision transformers. In *Proceedings of the IEEE/CVF International Conference on Computer Vision (ICCV)*, pages 9650–9660, 2021.

[37] Maxime Oquab, Timothée Darcet, Théo Moutakanni, Huy Vo, Marc Szafraniec, Vasil Khalidov, Pierre Fernandez, Daniel Haziza, Francisco Massa, Alaaeldin El-Nouby, et al. DINOv2: Learning robust visual features without supervision. *Transactions on Machine Learning Research*, 2024. arXiv:2304.07193.

[38] Oscar Mañas, Alexandre Lacoste, Xavier Giró-i Nieto, David Vázquez, and Pau Rodríguez. Seasonal contrast: Unsupervised pre-training from uncurated remote sensing data. In *Proceedings of the IEEE/CVF International Conference on Computer Vision (ICCV)*, pages 9414–9423, 2021.

[39] Yi Wang, Nassim Ait Ali Braham, Zhitong Xiong, Chenying Liu, Conrad M. Albrecht, and Xiao Xiang Zhu. SSL4EO-S12: A large-scale multimodal, multitemporal dataset for self-supervised learning in Earth observation. *IEEE Geoscience and Remote Sensing Magazine*, 11(3):98–106, 2023. doi: 10.1109/MGRS.2023.3281651.

[40] Yezhen Cong, Samar Khanna, Chenlin Meng, Patrick Liu, Erik Rozi, Yutong He, Marshall Burke, David B. Lobell, and Stefano Ermon. SatMAE: Pre-training transformers for temporal and multi-spectral satellite imagery. In *Advances in Neural Information Processing Systems*, volume 35, 2022.

[41] Colorado J. Reed, Ritwik Gupta, Shufan Li, Sarah Brockman, Christopher Funk, Brian Clipp, Kurt Keutzer, Salvatore Candido, Matt Uyttendaele, and Trevor Darrell. Scale-MAE: A scale-aware masked autoencoder for multiscale geospatial representation learning. In *Proceedings of the IEEE/CVF International Conference on Computer Vision*, 2023.

[42] Daniela Szwarcman et al. Prithvi-EO-2.0: A versatile multi-temporal foundation model for Earth observation applications, 2024. URL https://arxiv.org/abs/2412.02732. arXiv:2412.02732.

[43] Guillaume Astruc, Nicolas Gonthier, Clement Mallet, and Loic Landrieu. AnySat: An Earth observation model for any resolutions, scales, and modalities. *arXiv preprint arXiv:2412.14123*, 2024.

[44] Shubham Choudhury et al. REJEPA: A novel joint-embedding predictive architecture for efficient remote sensing representation learning. In *Proceedings of the IEEE/CVF Conference on Computer Vision and Pattern Recognition Workshops (EarthVision)*, 2025.

[45] Matteo Berti et al. RER2023: The landslide inventory dataset of the May 2023 Emilia-Romagna meteorological event. *Earth System Science Data*, 17:1055–1074, 2025. doi: 10.5194/essd-17-1055-2025.

[46] Tete Xiao, Yingcheng Liu, Bolei Zhou, Yuning Jiang, and Jian Sun. Unified perceptual parsing for scene understanding. In *Proceedings of the European Conference on Computer Vision*, pages 418–434, 2018.

[47] Albert Gu and Tri Dao. Mamba: Linear-time sequence modeling with selective state spaces. *arXiv preprint arXiv:2312.00752*, 2023.

[48] Lianghui Zhu, Bencheng Liao, Qian Zhang, Xinlong Wang, Wenyu Liu, and Xinggang Wang. Vision mamba: Efficient visual representation learning with bidirectional state space model. In *Proceedings of the 41st International Conference on Machine Learning (ICML)*, pages 62429–62442, 2024.

[49] Enze Xie, Wenhai Wang, Zhiding Yu, Anima Anandkumar, Jose M. Alvarez, and Ping Luo. SegFormer: Simple and efficient design for semantic segmentation with transformers. In *Advances in Neural Information Processing Systems*, volume 34, pages 12077–12090, 2021.